Original Article

Optimal EV Charging Using ANT Lion Optimized ANN Based MPPT with High Gain Modified Zeta Converter

S.L. Sreedevi[1], B.T. Geetha[2]

[1,2]*Department of Electrical and Electronics Engineering, Saveetha School of Engineering, SIMATS, Saveetha University, Tamilnadu, India.*

[1]*Corresponding Author : sreeperiit1362@gmail.com*

Abstract - Photovoltaic (PV) based power systems can be integrated with charging loads for Electric Vehicles (EVs) owing to their similar power forms, interfaces, and locations. Due to the random nature of solar generation and EV charging, this integration involves a high level of uncertainty, which demands robust control design and optimization to provide a constant power supply to the EV battery. Therefore, this research implements a novel optimized Artificial Neural Network based Maximum Power Point Tracking (ANN-MPPT) with High gain DC to DC converter for efficient EV battery charging. A high-gain modified Zeta converter is deployed to convert the minimal voltage output of PV to a higher level of increased voltage. To maximize the power from the PV panel, the Ant Lion Optimized ANN (ALO-ANN) based MPPT is established in this work, which helps to preserve the stabilized DC link voltage. DC-AC conversion is accomplished using the High Frequency (HF) full bridge inverter, which provides a regulated high output voltage. Similarly, the HF isolation transformer operates to convert power while ensuring sufficient voltage balancing and galvanic isolation. A Proportional Integral controller (PI) is implemented to control the output of a proposed interleaved synchronous rectifier, which achieves the highest possible output to the battery for EVs by decreasing HF rectification losses while providing quicker transition response and input noise rejection. Furthermore, the proposed system's functionality is validated by employing MATLAB simulation. According to the computational findings, the proposed system has a high-efficiency value of 93.6% and a better transient response to the system.

Keywords - Ant Lion Optimized ANN-based MPPT, EV battery, HF isolation transformer, High Frequency full bridge inverter, High gain modified zeta converter, PV system.

1. Introduction

Electric Vehicles (EVs) are ecological, scientific, and financial benefits that have accelerated the incorporation of energy sources and transportation networks in previously inconceivable ways [1, 2]. The primary connection between the two industries is the battery charge, which supplies the control, traction, air conditioning, and lighting systems for electric vehicles. Nevertheless, using the power grid to charge the EV puts more pressure on the utility, especially during excessive demand.

Encouraging clean energy sources for charging is one viable option for minimizing the negative impact on the electrical grid [3]. This type of green power aims to reduce adverse ecological impacts while increasing the total efficacy of charging systems. Solar power is becoming more commonly regarded as an environmentally friendly option for boosting electrical energy as the average price of PV modules keeps decreasing [4]. In addition, the PV system is practically free of maintenance in terms of both labour and fuel. PV-based EV charging has been boosted further by advancements in

power conversion technology, battery management techniques, and increased deployment adheres to specifications for design [5].

Numerous studies on the PV-based EV battery charging system have been reviewed; some of those research works are discussed in the section below. In [6], the author proposes an instantaneous EV charging management approach that employs short-term PV power forecasting and IBGWO. Furthermore, the suggested technique can enhance PV power utilization while lowering operator electricity costs.

This study does not consider the cost and durability of ESSs and PVs. The author describes a Finite Horizon Markov Decision Process (FHMDP) framework for the most effective PV-supported EVCS management [7, 8]. The indicated finite-horizon MDP model minimizes the overall operating expenses of the PV-assisted EVCS. However, because regular routines and charging infrastructure limit EV users, it is challenging to encourage them personally. The author discussed PV-owned stations equipped with an ESS in [9, 10]. This method requires

far less computing time than the centralized method. Though the centralized technique can provide the best response, choosing takes a long time, especially when there are many EVs.

Reference [11] uses a PSO to regulate the best size for the ESU PV array for EVs' PV grid-linked charging system. This effort is intended to accurately calculate the optimal size of the EV charging station's elements. However, the energy transmission from PV to ESU fluctuates depending on the circumstances.

In reference [12], the author proposes a four-stage optimization and control method for lowering the maintenance expenses of an incorporated intelligent charging station. This control strategy improves the system's operating performance. However, employing hour-ahead data in the suggested technique may cost more significantly.

In this work [13], an agent-based strategy founded on NetLogo impacts the load demand caused by EV charging. This expands the possibility of analyzing the influence of shifting peak timings on EV charging load demand. However, a sensitivity evaluation with a broader range of factors is required. This work is based on the author's presentation of a unique bi-level optimum dispatch framework for the EVCS with a CIES in multi-stakeholder situations [1].

A thorough V2G scheduling model, on the other hand, would be a more realistic option. However, this is a low-efficiency computation. The reference [14] describes the design of a storage battery, PV array, grid, and DG set-based

charging infrastructure for EV charging. It enhances the likelihood of MPP functioning of the PV array.

Nevertheless, the solar PV panel remains inoperable because of a single mode of functioning in the grid-connected state. Optimization methodology for Fast EV Charging Stations (FECSs) is provided in [15]. This optimization framework provided an intuitive understanding of the selection of variables for actual-world instances, leading to a successful choice about the cost of FECS. However, the role of FECS in distribution networks and how it affects power quality will be crucial.

Hence, this paper proposes a high-gain modified zeta converter and ALO-ANN-based MPPT for a PV-powered EV charging system. The lower PV voltage output is converted to its boosted form using a high-gain modified zeta converter. Adopting ALO-ANN-based MPPT maximizes PV panel power, and the converter's uncontrolled DC output voltage becomes stable with distortion-free output. According to the simulation results, the proposed system obtains an optimal efficiency value of 93.8%. Detailed explanations of the proposed system can be found in the following section.

2. Proposed System Description

Using clean energy sources, including PV, to charge EVs is a fascinating choice that provides various economic and technical benefits. The problems associated with greenhouse emissions caused by gasoline and diesel engines can be decreased by integrating emission-free EVs with carbon-free solar energy production. Figure 1 illustrates the proposed system's block diagram.
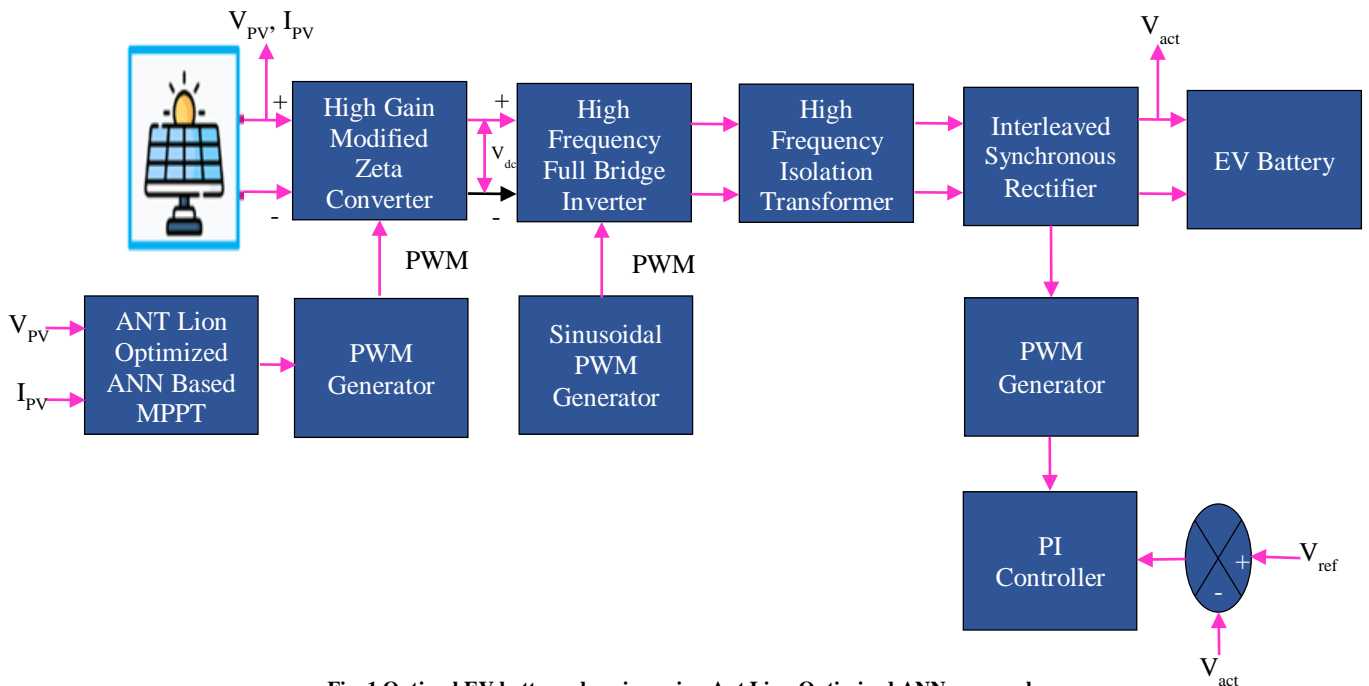

Fig. 1 Optimal EV battery charging using Ant Lion Optimized ANN approach

The high gain modified zeta converter increases the PV's poor voltage output V_{PV}. Because of the fluctuating nature of solar power, the converter's voltage output fluctuates and isn't consistent. An ALO-ANN-based MPPT control strategy ensures that the converter output is steady and distortion-free. It also extracts the utmost power from the PV panel. The output DC voltage is sent into a high-frequency full bridge inverter, helping the DC-AC conversion process. A sinusoidal PWM generator is deployed to generate PWM pulses for inverter circuit functioning.

The resultant alternating current supply is supplied into an HF isolation transformer that prevents the entire system from shocks caused by electricity. The interleaved synchronous rectifier is powered by an alternating current supply, which is then transformed into a DC voltage. The analyzed output from V_{ref} and V_{act} is supplied to the PI controller, which controls the voltage of the interleaved synchronous rectifier. Subsequently, an integrated synchronous rectifier converts sinusoidal voltage to a comparable DC voltage to improve the system's effectiveness in EV battery charging.

3. Proposed System Modelling
3.1. PV Modelling
Overall, PV devices convert sunlight into electrical power. A cell is a single PV device. PV cells are placed in parallel and series to create a solar energy system. The amount of parallel and series cells determines the solar power system's voltage and current. Because PV arrays are nonlinear devices, the analogous circuit framework, shown in Figure 2, is widely used to activate their characteristics.

The general equation of PV panel is given by:

$$I_{pv} = I_{sh} - I_d - I_p \qquad (1)$$

I_d is the current passing via the diode and I_p is the current entering via the resistance parallel to the circuitry, and Equations (2) and (3) of the previous equation provide these values correspondingly.

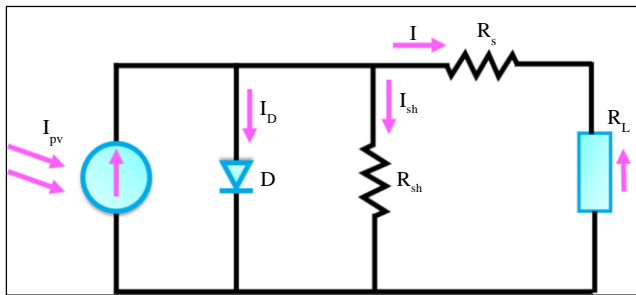$$I_d = I_O \left[exp \left(V + \frac{IR_s}{aV_T} \right) - 1 \right] \qquad (2)$$

Fig. 2 PV panel circuit

$$I_p = \left(V + \frac{IR_s}{R_p} \right) \qquad (3)$$

By including Equation (2) and Equation (3) in Equation (1), the attained equation is:

$$I_{pv} = I_{sh} - I_O \left[exp \left(V + \frac{IR_s}{aV_T} \right) - 1 \right] - \left(V + \frac{IR_s}{R_p} \right) \qquad (4)$$

At all testing circumstances, the I-V and P-V curves can be determined using the entire unique equation of the PV panel framework, Equation (4), which contains independent variables. The steady voltage that comes from the PV panel is adjusted using an appropriate converter. Following is an explanation of the high-gain modified zeta converter used in this work.

3.2. Modelling of High Gain Modified Zeta Converter
The paper proposes a high-gain modified zeta converter to increase the PV panel's output DC voltage, which is more advantageous, including a significant power factor ratio that reduces controller complexity and precisely controls the output voltage.

The proposed high-gain modified zeta converter is also superior to traditional DC-DC converters in reduced switching stress, simplified controller circuits, better switching prevention, precise output, and medium-power quality characteristics. Figure 3(a) depicts the high gain modified zeta converter circuit diagram.

3.2.1. Modes of Operation
Stage I
Figure 3(b) depicts the corresponding circuit for this mode. In this state, the switch is activated, and the inductors can store power (L₁, L₂) and capacitor (C_{in}). I_{L1}, I_{L2} and V_{cin} have been assigned higher values. Additionally, because the diode is in the non-conducting stage, the energy that is stored in the C_o, it is released to the load. The C_{in} capacitor is initially charged downwards, increasing the voltage over it. When the diode's current drops to zero, the C_o capacitor supplies the necessary power to the load.

Stage II
Figure 3(c) depicts the corresponding circuit for this mode, and the switch is disabled in that state. I_{L1} is growing while I_{L2} and V_{cin} are starting to decline as the capacitor C_{in} starts to be released. When the power switch is turned off in this state of operation, the capacitor C_{in} discharges and the current via L_1 rises. In contrast, the voltage across C_{in} and the current flowing via the inductor L_2 have dropped. With the conduction diode D_o, the capacitor C_o, begins to charge, and the sum of the two diode currents, I_{L1} and I_{L2} is the diode current. The method continues till $V_{cin} = V_{co}$.

Stage III

Figure 3(d) portrays the corresponding circuit for this mode of operation. In this scenario, L_1 and L_2 are used to discharge the V_{cin}, V_{co}, and V_{cin}. In this state, L_2 discharges across the diode to charge C_o, resulting in a drop in I_{L2} and a rise in V_2. As charging begins, the current I_{L1} remains active, and this state of operation lasts till $I_{L2} = 0$.

$$V_{out} = \frac{D_{duty}}{1-D_{duty}} V_{in} \qquad (5)$$

$$L_1 = \frac{V_S D_{duty}}{\eta_e I_S F_{switch}} = \frac{R_{IN} D_{duty}}{\eta_e F_{switch}} = \frac{V_S^2 D_{duty}}{P_S \eta_e F_{switch}} = \frac{1}{\eta_e F_{switch}} \times \frac{V_S^2}{P_S} \times \frac{V_{out}}{V_S + V_{out}} \qquad (6)$$

$$L_2 = \frac{V_{out} \times 1 - D_{duty}}{2.I_{L_B}.F_{switch}} = \frac{V_{out} D_{duty}}{2 I_{L_A}.F_{switch}} = \frac{R_{IN} V_{out} D_{duty}}{2.V_S.F_{switch}} = \frac{V_S^2}{P_S} \times \frac{V_{out}}{2.V_S.F_{switch}} \times \frac{V_{out}}{V_S + V_{out}} \qquad (7)$$

$$C_{in} = \frac{V_{out} D_{duty}}{K_R.V_{C_A}.F_{switch}.R_{Load}} = \frac{V_S}{K_R.F_{switch}.(V_S + V_{out}^2)} = \frac{V_{out} \times (V_{out}/(V_S + V_{out}))}{K_R \times V_{out} + V_S \times F_{switch} \times \left(V_{out}^2 / P_S\right)} \qquad (8)$$

$$C_o = \frac{I_{C_B}}{2\omega_{switch}.V_{out}} = \frac{P_S/V_{out}}{2\omega_{switch}\delta_R V_{out}^2} \qquad (9)$$

Where δ_R is capacitor ripple factor.
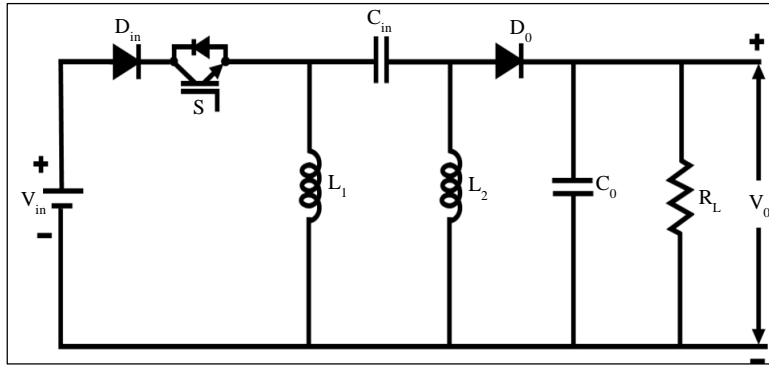

Fig. 3(a) Proposed high gain modified zeta converter
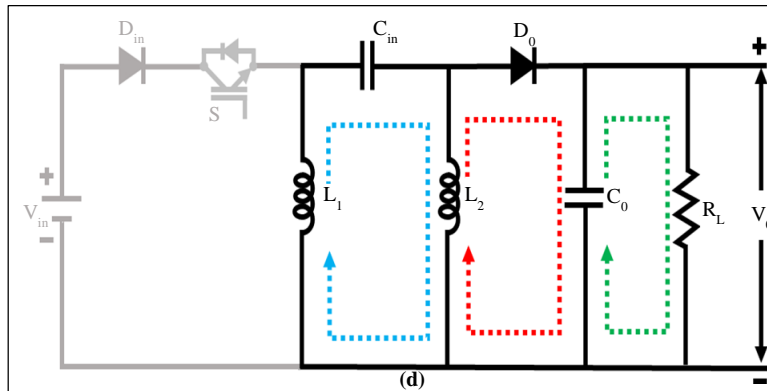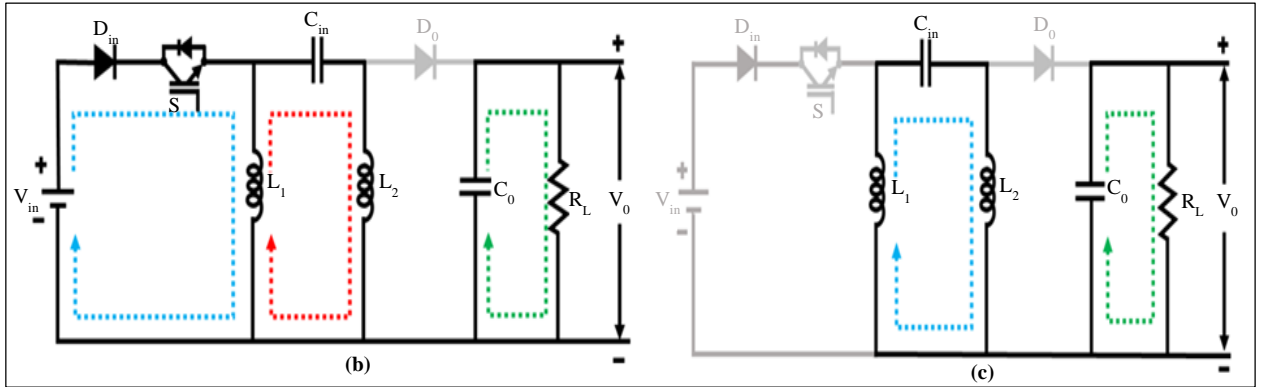

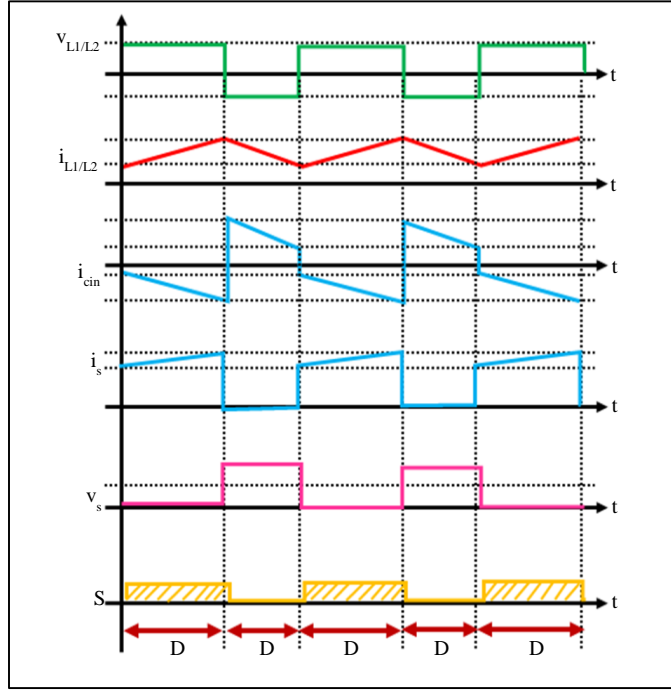**Fig. 3(b) Stage 1, (c) Stage 2, and (d) Stage 3.**

Fig. 4 Timing waveforms of the proposed converter

The proposed high-gain modified zeta converter timing waveform is illustrated in Figure 4. The modelling of ALO – ANN-based MPPT is explained in the forthcoming section.

3.3. Modelling of Ant Lion Optimized ANN Based MPPT

This paper presents a unique MPPT method based on optimized ANN using the Ant Lion algorithm. The ALO is provided to tune the variables of the ANN approach. The provided MPPT technique is employed to efficiently observe the MPP of a PV system under varying temperature and intensity circumstances. The following section offers an in-depth description of the proposed MPPT controller.

3.3.1. ANN -MPPT Controller

On the I/V curves of solar energy systems, there is a specific region referred to as the MPP, whereby the system operates most effectively and produces the most significant amount of power. A power converter-equipped MPP control is used to maintain the PV array's functioning limit at the MPP. The MPPT control system regulates the PV panel current or voltage without considering the load as a way to accomplish this.

Voltage from solar panels is used as a control parameter, and based on voltage, an MPPT controller is developed. The system operates at MPP by estimating the reference voltage (V_{MPP}) utilizing ANN. This voltage relies on the system's solar irradiation (G) and cell temperature (T). A correlation between the inputs (G and T) and output (V_{MPP}) has been identified and employed to produce the data set for the ANN training.
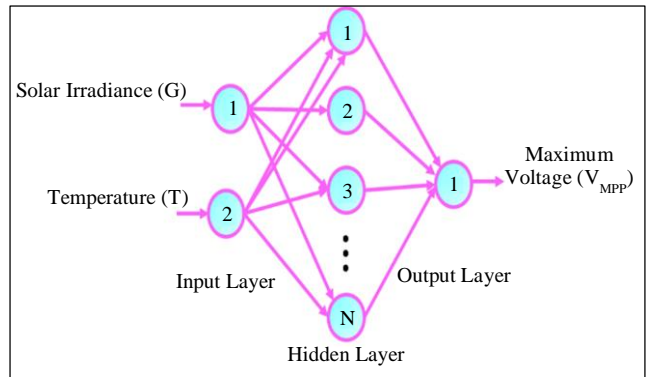

Fig. 5 ANN-based MPPT framework

Figure 5 depicts the developed ANN layout, which contains an output layer, a hidden layer and an input layer composed of an ANN-based MPPT framework.

3.3.2. Ant Lion Optimization Algorithm

The ALO can imitate ant lions' natural ways of hunting. An ant lion travels in a circle to create a hole in the sand. The pupae of the ant lion cover-up in the pit's bottom (their trap) and await for ants (their prey). When the prey (ant) shows up, the ant lions pull it into the pit by flinging sand toward the opening. The subsequent presumptions form the foundation of the effectiveness of the algorithm.

1. In the process of searching space, ants-the prey-move randomly, and the ant lion traps impact the way they travel.
2. The optimal ant lion fitness leaves a big hole.

3. An outstanding ant lion's capacity to chase an ant is directly related to its fitness level.
4. Every ant lion in each cycle can pursue any ant.

The ant lions can pursue down the bound ants in a hole. Ants change their positions throughout the search space by taking random walks.

$$X_t = [0, cumsum(2r_t(t_1) - 1), cumsum(2r_t(t_2) - 1) \dots \dots \dots cumsum(2r_t(t_n) - 1)] \tag{10}$$

Where n is the maximum amount of iterations, n is the population size, t is the random walk's step, cumsum is the cumulative sum, and r is the stochastic function, which is calculated using the subsequent equation.

$$r(t) = \begin{bmatrix} 1 \leftarrow if(rand > 0.5) \\ 0 \leftarrow if(rand \leq 0.5) \end{bmatrix} \tag{11}$$

The flowchart of ALO-optimized ANN is represented in Figure 6. Equation (11) ensures that the ants stay inside the search space's boundary.
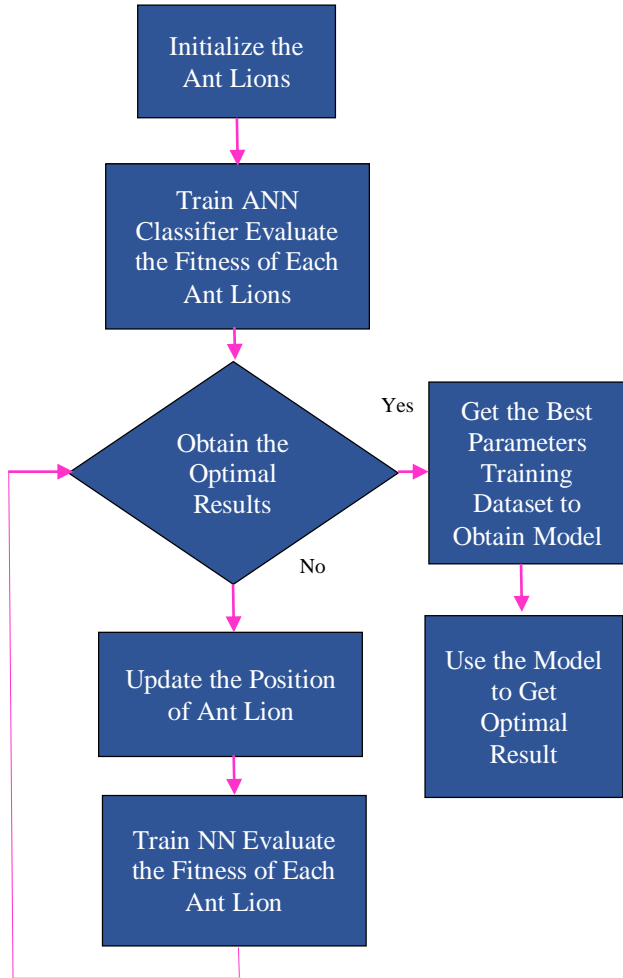

Fig. 6 ALO optimized ANN flowchart

$$R_t^j = \frac{(X_i - a_i^t) \times (d_i^t - c_i^t)}{(b_i^t - a_i)} + c_i^t \tag{12}$$

R_t^j is the location of anti i after conducting a random walk to a nearby ant lion j, wherein at i is the smallest step of Randomized Walk (RW), X_i^t is the location of ith anti at t th iteration, b_i is the greatest step of the random walk, The most minor ith variable at the tth iteration is c_i^t, while the maximum ith variable is d_i^t. The above concept is analytically modelled using the following equation.

$$d_i^t = Ant\ lion_j^t + d^t \tag{13}$$

$$c_i^t = Ant\ lion_j^t + c^t \tag{14}$$

Where d^t is the greatest value of every factor at the t th iteration and d_i^t is the greatest of all variables for the ith ant. c^t is the minimum of all variables at the tth iteration.

$$c^t = \frac{c^t}{I} \tag{15}$$

$$d^t = \frac{d^t}{I} \tag{16}$$

When I is the ratio, d^t is the highest value of all variables at the t th iteration, and c^t is the lowest value of all variables at the t th iteration.

The ant lion needs to modify the tracked ant's location to maximize its probability of capturing additional ant lion. Equation (17) simulates this occurrence.

$$Ant\ lion_j^t = \begin{bmatrix} Ant_i^t \leftarrow if\left(f(Ant_i^t)\right) < \left(f(Ant\ lion_i^t)\right) \\ Ant\ lion_j^t \leftarrow otherwise \end{bmatrix} \tag{17}$$

Where t is the present iteration, Ant_i^t is the initial position of the ith ant lion and Ant_i^t is the position of the jth ant lion.

Every iteration's elite ant lion is the one with the highest level of fitness. To determine where the ants will be, apply the equation below.

$$Ant_i^t = \frac{R_A^t + R_e^t}{2} \tag{18}$$

Where Ant_i^t is the position of the ith ant lion at the current iteration, R_e^t is the randomized path around the elite ant lion at the current iteration, and R_A^t is the randomized walk around the ant lion selected by the Roulette Mechanism (RM).

3.4. Modelling of High-Frequency Full Bridge Inverter
As illustrated in Figure 7, an inverter with voltage sources is similar to a full bridge inverter. A two-line DC input supply is enough. Controlling the ON and OFF states of thyristors,

allowing the frequency of their output to be changed. This inverter's output circuitry is made up of 4 thyristors. T_1 to T_4, a two-wire DC source V_s, and four diodes D_1 to D_2. Every thyristor and diode is wired in the reverse direction. The block diagram below depicts the electrical circuit schematic for a full bridge inverter. Turning the thyristor ON and OFF is not illustrated in the circuit design for ease of use. Every thyristor only runs when a gate signal is there; when a pulse is not present, the thyristors turn off. This means that thyristors. T_3 and T_4 are turned on for half of the time duration, then T_1 and T_2 are turned on for the following cycle.

Two thyristors are turned on in half the time. T_1 and T_2 thyristors are engaged for an identical time of $T/2$. Since T_1 and T_2 are used to link the load to the source, the load and source voltage remain positive. As a result, the output voltage waveform shows the load voltage as positive and equivalent to V_s. When the gate signals (i_{g1} and i_{g2}) has been eliminated, T_1 and T_2 remain turned off. T_3 and T_4 are turned on as a consequence of instant gate signals (i_{g3} and i_{g4}).

When T_3 and T_4 function properly, the load is connected to the source. V_s indicates the amount of the load voltage again; however, this time, its direction is inverted. As a result, the output voltage is displayed negatively in the voltage waveform. Furthermore, Thyristors T_1 and T_2 are running for time $0 < t \leq T/2$ and the load voltage is V_s. Thyristors T_3 and T_4 conduct for $(\frac{T}{2}) < t \leq T$ and the load voltage I s$V_0 = -V_s$. Figure 8 depicts the waveforms of a full bridge inverter's output voltage and gating signal.
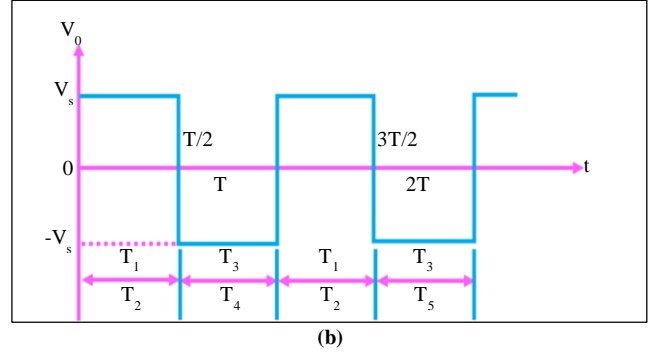

Fig. 7 Power circuit for full bridge inverter

(a)

(b)
Fig. 8 Full bridge inverter waveforms (a) Gate signal, and (b) Output voltage.

The high-frequency isolation transformer used in the present research is described below.

3.5. Modelling of High-Frequency Isolation Transformer

Rectifiers convert alternating current input voltage to direct current output voltage. The inverter turns DC power towards an HF switching pulse at that time. The high-frequency transformer presented in this work can divide output and input and avoid 3n-order harmonics because of its star-delta structure. Figure 9 depicts the isolation transformer conceptual diagram. This proposed research uses the isolated transformer to divide the HF full bridge inverter and circuits for rectifiers. Isolation transformers offer galvanic isolation because there is no conducting path between load and source. This isolation is employed to provide power across two separate circuits, prevent electric shock, and minimize noise from electricity in critical electronics.

The transformer's basic electromagnetic equation is expressed as,

$$U = 4.44 \cdot N \cdot \phi_{max} \cdot f \qquad (19)$$

Where N indicates primary turns, U represents primary voltage, ϕ_{max} represents maximum magnetic flux, and f indicates frequency.
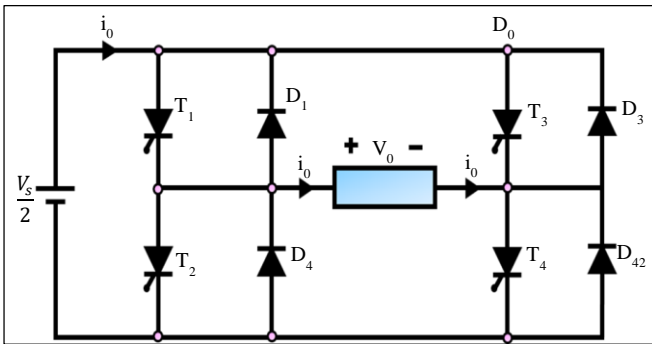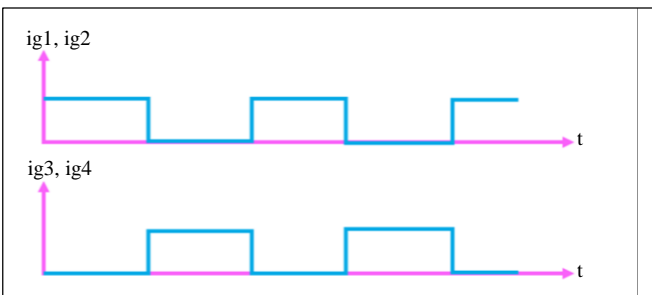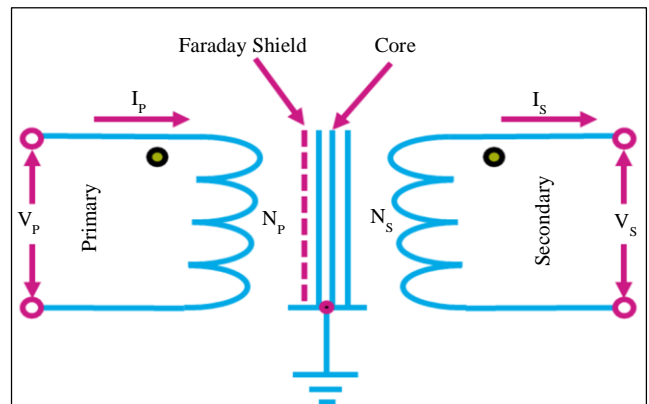

Fig. 9 Isolation transformer

By enhancing system frequency when voltage obtained is constant, N is decreased, and flux is represented as,

$$\phi_{max} = B_{max} \cdot S \qquad (20)$$

Where the core leg's cross-section is indicated by S.

The cross-section of the core leg shrinks, as does the coil's length and the core's volume. A reduced core window region results from fewer revolutions. The transformer is going to be smaller and lighter, requiring fewer components. Three-phase systems have a higher power density than single-phase systems.

In classic EV quick chargers, industrial frequency transformers are often composed of silicon steel. Though cheap, degradation makes it hard to use at frequencies above 2 kHz. Finally, the AC output voltage obtained from the HF isolation transformer is converted into the DC output voltage by using an interleaved synchronous rectifier with the assistance of the PI controller. The obtained stabilized actual voltage V_{act} is supplied to the EV battery charging system with improved efficiency. The attained results of the proposed system are explained elaborately in the following section.

4. Results and Discussion

This research proposes a high-gain modified zeta converter and an ALO-ANN-based MPPT-based PV-powered EV charging system. Employing a high-gain modified zeta converter, the lower voltage output of PV turns to a considerably higher voltage. PV panel power is maximized, and the converter's uncontrolled DC output voltage becomes constant using ALO-ANN-based MPPT. According to the simulation results, the proposed system reaches an ideal efficiency value of 93.8%. Table 1 provides the proposed system's parameter specifications.

It is evident from the waveform analysis in Figure 10(a) that the temperature remained constant at 35°C, and it is possible to examine the proposed approach's effectiveness in dealing with the erratic behaviour of the solar panel system. Similarly, Figure 10(b) demonstrates how a PV system can irradiate 1000 W/Sq.m. Figure 11 displays the simulated waveform, which shows a PV system's resultant current and voltage. A voltage of 60V is kept constant from the PV panel, and after reaching a peak value of 760 for 0.15 seconds, the current begins to vary regarding its inconsistent nature. The proposed high-gain modified zeta converter maximizes the PV voltage that is produced.

Table 1. Parameter description

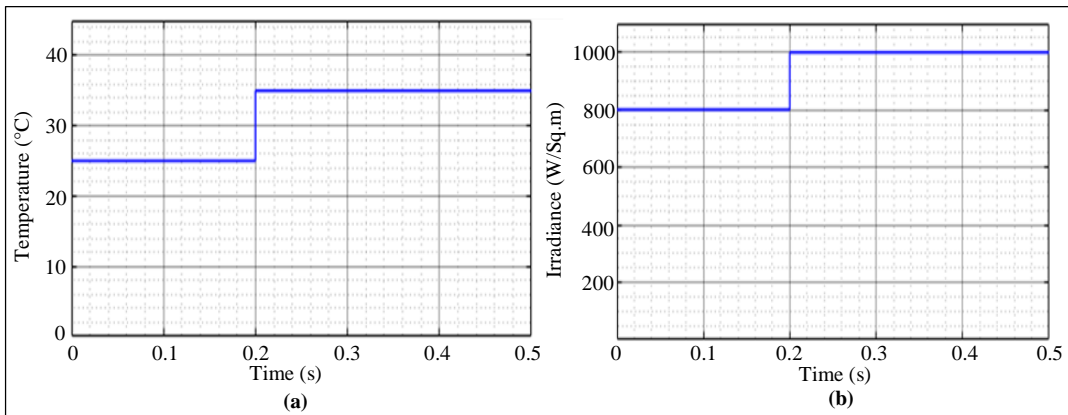| Parameters	Descriptions
PV System	
Short Circuit Current	8.3A
Peak Power	10KW, 10 Panels
Series Connected Solar PV Cells	36
Open Circuit Voltage	12V
High Gain Modified Zeta Converter	
L_1L_2	1.2mH
C_{in}	4.7μF
C_o	2200 μF
Isolation Transformer	1:0.5
Switching Frequency	10KHz

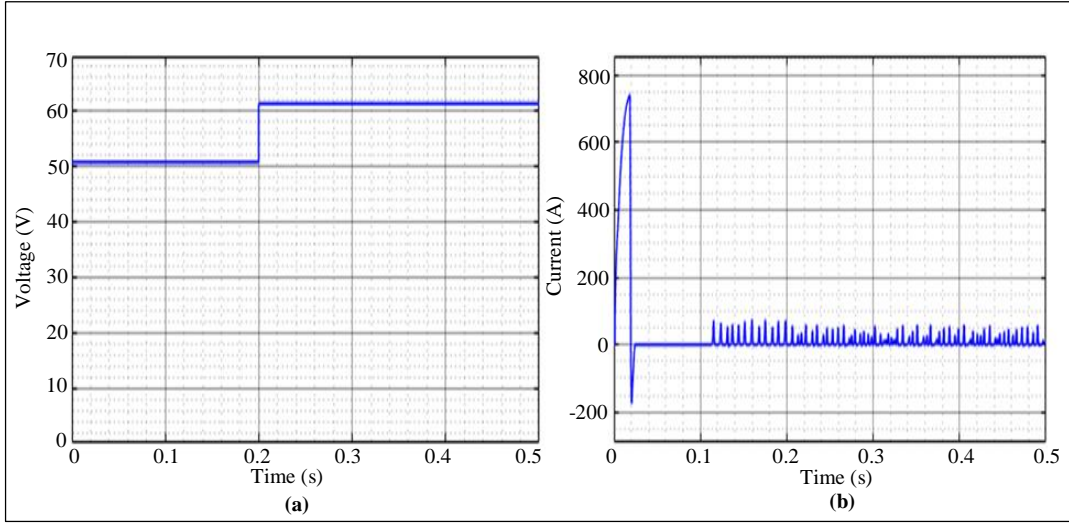**Fig. 10 Waveforms indication of solar panel (a) Temperature, and (b) Irradiation.**

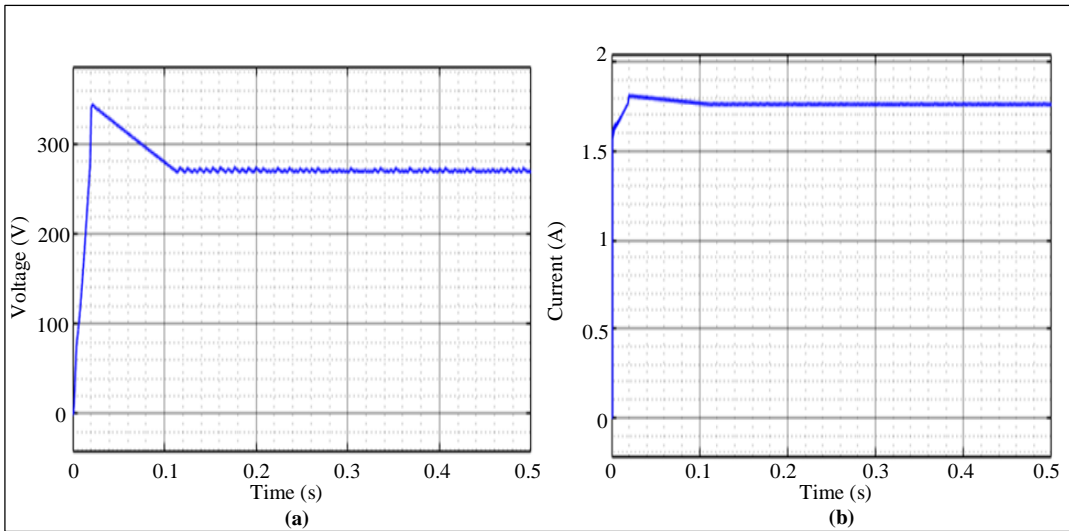**Fig. 11 Waveforms indication of solar panel (a) Voltage, and (b) Current.**

Fig. 12 Waveforms indication of high gain modified zeta converter output (a) Voltage, and (b) Current.
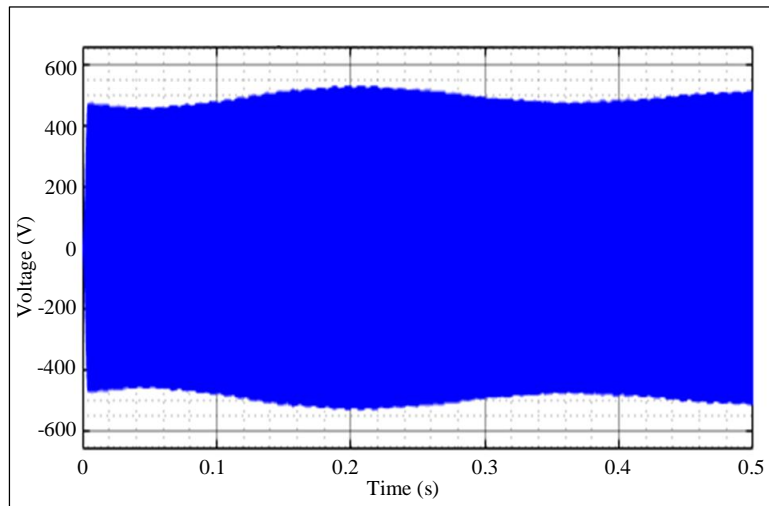

Fig. 13 High-frequency inverter voltage waveform

The output current and voltage waveforms of the high gain modified converter are displayed in Figure 12. From the waveform, the constant 280V is attained after 0.15 seconds with minor distortions. Similarly, the current remains stable at a value of 1.8A after 0.03 sec. Figure 13 indicates the waveform of high-frequency inverter voltage; here, the voltage varies from within the range of -450V to 450V.

The DC output voltage of the synchronous rectifier is denoted in Figure 14. The constant output DC voltage of 98V is obtained by both synchronous rectifiers 1 and 2. With the implementation of the PI controller, the stable output DC

voltage value of 198V of interleaved synchronous rectifier is attained, illustrated in Figure 15.

Figure 16 displays the waveforms of the EV battery. Figure 16(a), which shows the voltage waveform for the battery, demonstrates how the voltage is consistently preserved at 198V over the system. In Figure 16(b), the current waveform illustrates that the current is kept constant at 1.5A over the system. Figure 16(c) displays the battery's SOC waveform, showing that the proposed system has reached 80% SOC. SOC is a percentage-based measure of the energy that a battery has on hand at any given time.
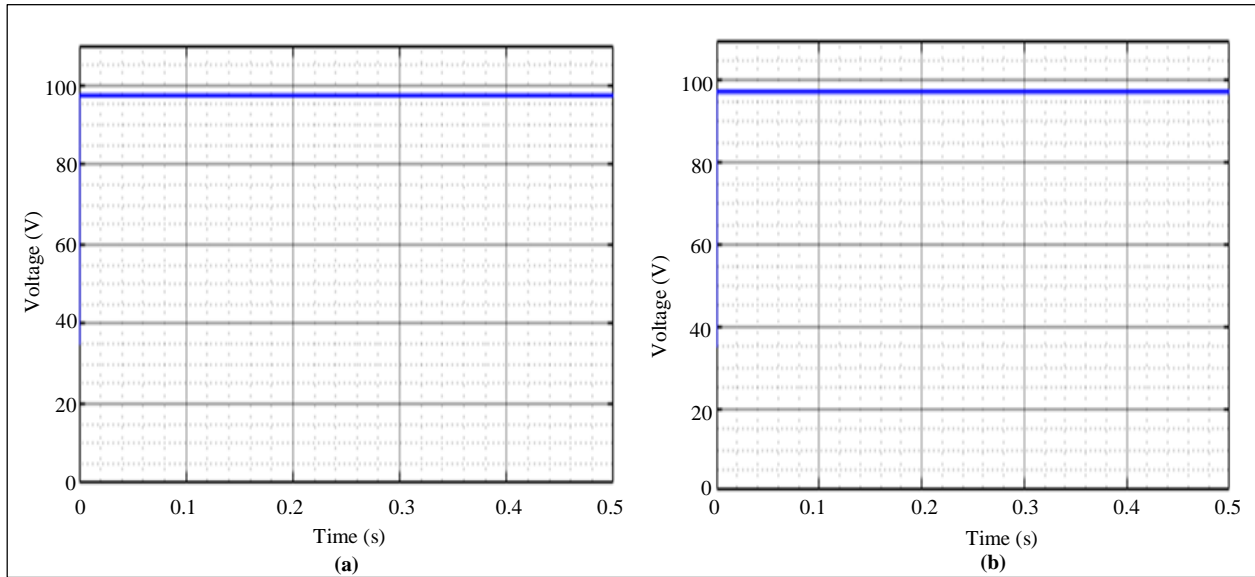

Fig. 14 Waveforms indication of output DC voltage (a) Synchronous rectifier 1, and (b) Synchronous rectifier 2.
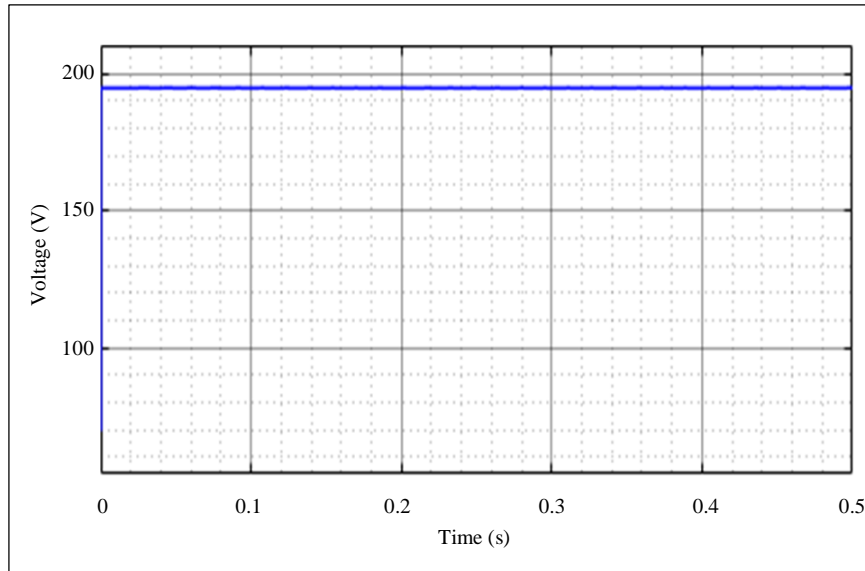

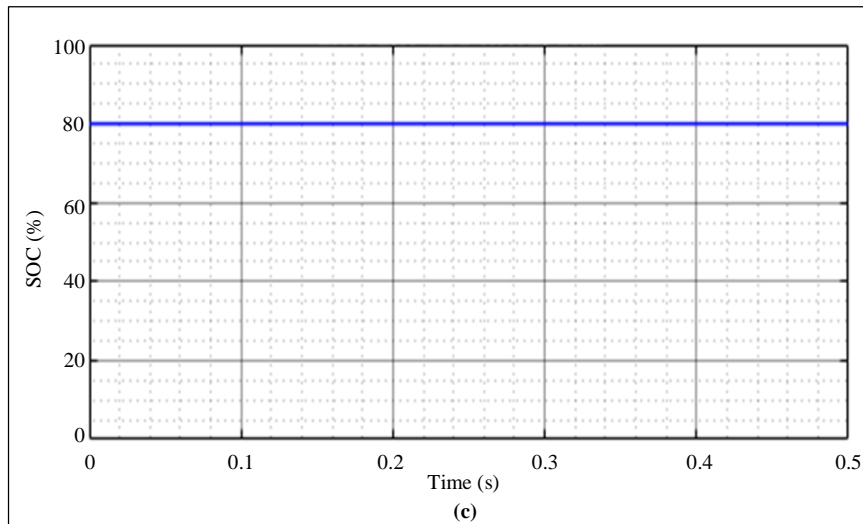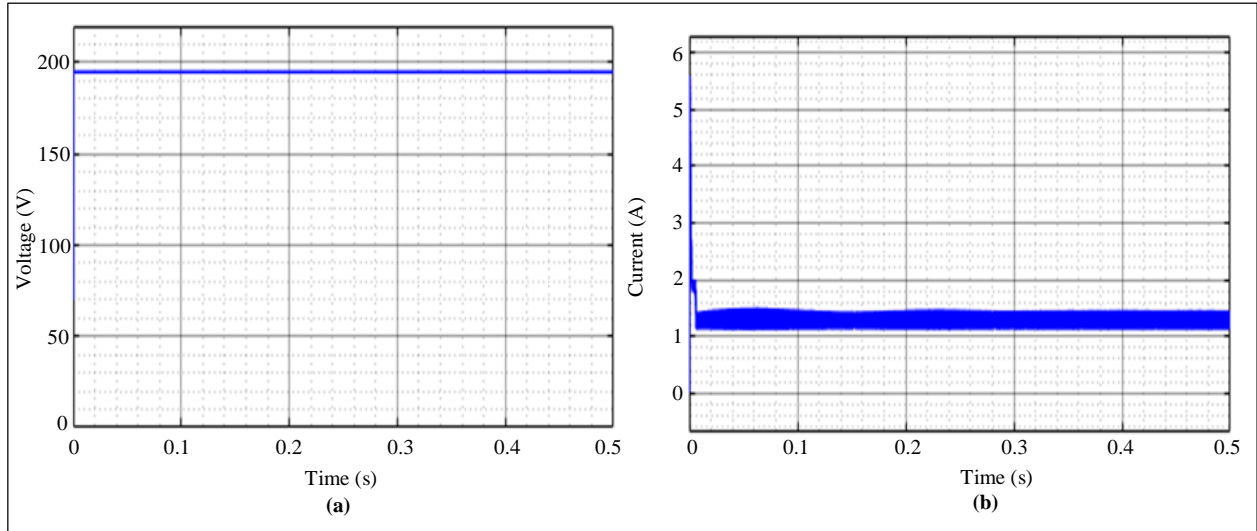**Fig. 15 DC voltage output of interleaved synchronous rectifier**

Fig. 16 Waveforms indication of EV battery waveforms (a) Voltage, (b) Current, and (c) SOC.

Converters	Efficiency (%)
Boost	80 [16]
Cuk	85 [17]
SEPIC	88.82 [18]
Proposed Converter	93.6%

Fig. 17 Comparison of efficiency %

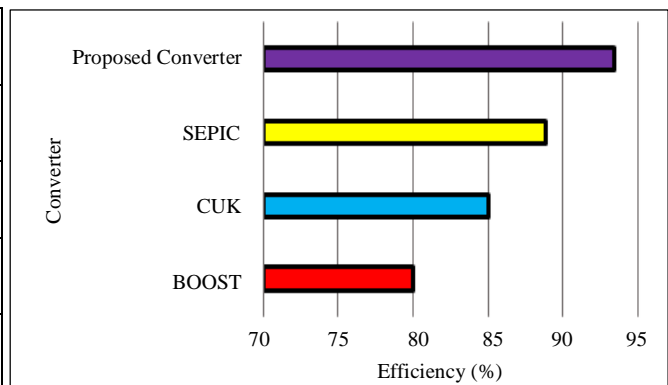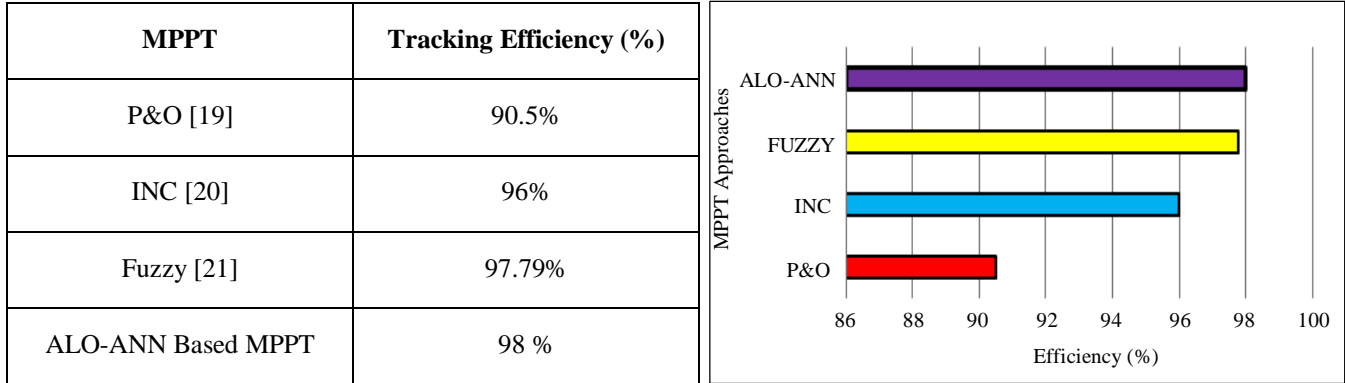| MPPT	Tracking Efficiency (%)
P&O [19]	90.5%
INC [20]	96%
Fuzzy [21]	97.79%
ALO-ANN Based MPPT	98 %

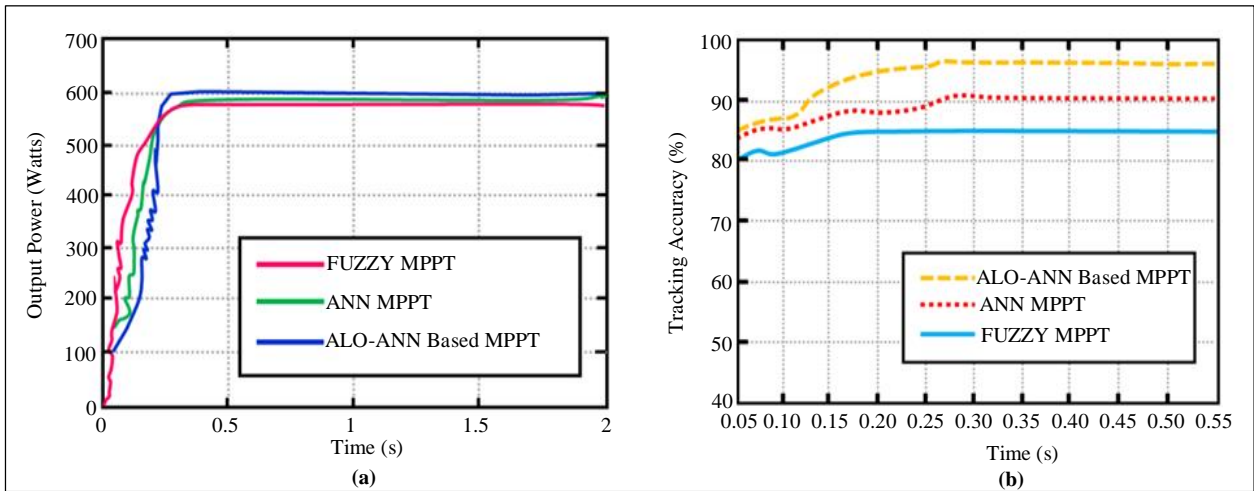**Fig. 18 Comparison of tracking efficiency %**

Fig. 19 Comparison of MPPT controller (a) Output power, and (b) Tracking accuracy.

4.1. Comparison Analysis

The comparison analysis of the proposed system with other existing approaches is provided below. The evaluation shows that the proposed system has maximum efficiency & tracking efficiency and high output power.

Figures 17 and 18 visually represent the efficiency of MPPT controllers and converters. In comparison to the conventional converters listed in [16-18] the proposed high-gain modified zeta converter performs superiorly, with an enhanced efficiency value of 93.6%, which is extremely considerable. Similar to how MPPT efficiency has improved, the ALO-ANN controller has 98% efficiency.

This efficiency is significantly greater than the controllers' efficiency values reported in [19-21]. Comparison analysis of MPPT controller tracking accuracy and output power is illustrated in Figure 19. The proposed ALO-ANN-based MPPT controller accomplishes high power output with an improved accuracy value of 97.6% compared to other approaches such as fuzzy and ANN MPPT.

5. Conclusion

This work employs a unique, optimized ANN-MPPT with a high-gain DC-DC converter for effective EV battery charging. A high gain modified Zeta converter is used to convert the lowest voltage output of PV into a higher level improved voltage. The ALO-ANN-based MPPT is developed in the present research to enhance the power from PV panels and help maintain the regulated DC link voltage.

The high-frequency full bridge inverter, which offers a controlled high output voltage, converts DC to AC. According to this, the HF isolation transformer converts power while ensuring enough voltage balance and galvanic isolation.

The output of a proposed interleaved synchronous rectifier is controlled by a PI controller, which increases the output to the battery for EVs by reducing HF rectification losses. Furthermore, the operation of the proposed system is verified by MATLAB simulation. According to the simulation results, the proposed system has an excellent efficiency value of 93.6% and a better dynamic response.

References

[1] Yang Li et al., "Coordinating Flexible Demand Response and Renewable Uncertainties for Scheduling of Community Integrated Energy Systems with an Electric Vehicle Charging Station: A Bi-Level Approach," *IEEE Transactions on Sustainable Energy*, vol. 12, no. 4, pp. 2321-2331, 2021. [CrossRef] [Google Scholar] [Publisher Link]

[2] Shakil Ahamed Khan et al., "A New Isolated Multi-Port Converter with Multi-Directional Power Flow Capabilities for Smart Electric Vehicle Charging Stations," *IEEE Transactions on Applied Superconductivity*, vol. 29, no. 2, pp. 1-4, 2019. [CrossRef] [Google Scholar] [Publisher Link]

[3] Zhaoxi Liu et al., "Transactive Real-Time Electric Vehicle Charging Management for Commercial Buildings with PV On-Site Generation," *IEEE Transactions on Smart Grid*, vol. 10, no. 5, pp. 4939-4950, 2019. [CrossRef] [Google Scholar] [Publisher Link]

[4] Hiroshi Kikusato et al., "Electric Vehicle Charging Management Using Auction Mechanism for Reducing PV Curtailment in Distribution Systems," *IEEE Transactions on Sustainable Energy*, vol. 11, no. 3, pp. 1394-1403, 2020. [CrossRef] [Google Scholar] [Publisher Link]

[5] Debasish Mishra, Bhim Singh, and Bijaya Ketan Panigrahi, "Sigma-Modified Power Control and Parametric Adaptation in a Grid-Integrated PV for EV Charging Architecture," *IEEE Transactions on Energy Conversion*, vol. 37, no. 3, pp. 1965-1976, 2022. [CrossRef] [Google Scholar] [Publisher Link]

[6] Wei Jiang, and Yongqi Zhen, "A Real-Time EV Charging Scheduling for Parking Lots with PV System and Energy Store System," *IEEE Access*, vol. 7, pp. 86184-86193, 2019. [CrossRef] [Google Scholar] [Publisher Link]

[7] Yu Wu et al., "Real-Time Energy Management of Photovoltaic-Assisted Electric Vehicle Charging Station by Markov Decision Process," *Journal of Power Sources*, vol. 476, pp. 1-16, 2020. [CrossRef] [Google Scholar] [Publisher Link]

[8] Peng Zhuang, "*Stochastic Energy Management and Cyber-Physical Security of Battery Energy Storage Systems in Smart Distribution Systems*," Thesis, University of Alberta, 2020. [CrossRef] [Google Scholar] [Publisher Link]

[9] Mohammad Ekramul Kabir et al., "Optimal Scheduling of EV Charging at a Solar Power-Based Charging Station," *IEEE Systems Journal*, vol. 14, no. 3, pp. 4221-4231, 2020. [CrossRef] [Google Scholar] [Publisher Link]

[10] Larissa Affolabi et al., "Optimal Transactive Energy Trading of Electric Vehicle Charging Stations with On-Site PV Generation in Constrained Power Distribution Networks," *IEEE Transactions on Smart Grid*, vol. 13, no. 2, pp. 1427-1440, 2022. [CrossRef] [Google Scholar] [Publisher Link]

[11] Abdul Rauf Bhatti et al., "Optimized Sizing of Photovoltaic Grid-Connected Electric Vehicle Charging System Using Particle Swarm Optimization," *International Journal of Energy Research*, vol. 43, no. 1, pp. 500-522, 2019. [CrossRef] [Google Scholar] [Publisher Link]

[12] Qin Yan, Bei Zhang, and Mladen Kezunovic, "Optimized Operational Cost Reduction for an EV Charging Station Integrated with Battery Energy Storage and PV Generation," *IEEE Transactions on Smart Grid*, vol. 10, no. 2, pp. 2096-2106, 2019. [CrossRef] [Google Scholar] [Publisher Link]

[13] Kalpesh Chaudhari et al., "Agent-Based Aggregated Behavior Modeling for Electric Vehicle Charging Load," *IEEE Transactions on Industrial Informatics*, vol. 15, no. 2, pp. 856-868, 2019. [CrossRef] [Google Scholar] [Publisher Link]

[14] Bhim Singh et al., "Implementation of Solar PV-Battery And Diesel Generator Based Electric Vehicle Charging Station," *IEEE Transactions on Industry Applications*, vol. 56, no. 4, pp. 4007-4016, 2020. [CrossRef] [Google Scholar] [Publisher Link]

[15] Leon Fidele Nishimwe H., and Sung-Guk Yoon, "Combined Optimal Planning and Operation of a Fast EV-Charging Station Integrated with Solar PV and ESS," *Energies*, vol. 14, no. 11, pp. 1-18, 2021. [CrossRef] [Google Scholar] [Publisher Link]

[16] Farzam Nejabatkhah et al., "Modeling and Control of a New Three-Input DC–DC Boost Converter for Hybrid pv/fc/Battery Power System," *IEEE Transactions on Power Electronics*, vol. 27, no. 5, pp. 2309-2324, 2012. [CrossRef] [Google Scholar] [Publisher Link]

[17] Francarl Galea et al., "Design of a High Efficiency Wide Input Range Isolated Cuk DC-DC Converter for Grid Connected Regenerative Active Loads," *World Engineers' Convention*, pp. 1-11, 2011. [Google Scholar] [Publisher Link]

[18] Patan Javeed et al., "SEPIC Converter for Low Power LED Applications," *Journal of Physics: Conference Series*, vol. 1818, pp. 1-12, 2021. [CrossRef] [Google Scholar] [Publisher Link]

[19] Hassanien Ramadan et al., "An Efficient Variable-Step P&O Maximum Power Point Tracking Technique for Grid-Connected Wind Energy Conversion System," *SN Applied Sciences*, vol. 1, pp. 1-15, 2019. [CrossRef] [Google Scholar] [Publisher Link]

[20] Nahla E. Zakzouk et al., "Improved Performance Low-Cost Incremental Conductance PV MPPT Technique," *IET Renewable Power Generation*, vol. 10, no. 4, pp. 561-574, 2016. [CrossRef] [Google Scholar] [Publisher Link]

[21] Doudou N. Luta, and Atanda K. Raji, "Fuzzy Rule-Based and Particle Swarm Optimisation MPPT Techniques for a Fuel Cell Stack," *Energies*, vol. 12, no. 5, pp. 1-15, 2019. [CrossRef] [Google Scholar] [Publisher Link]